

Control of concerted back-to-back double ionization dynamics in helium

Henrik R. Larsson^{1,2, a)} and David J. Tannor²

¹⁾*Institut für Physikalische Chemie, Christian-Albrechts-Universität zu Kiel, Olshausenstraße 40, 24098 Kiel, Germany*

²⁾*Department of Chemical Physics, Weizmann Institute of Science, 76100 Rehovot, Israel*

(Dated: 18 April 2022)

Double ionization (DI) is a fundamental process that despite its apparent simplicity provides rich opportunities for probing and controlling the electronic motion. Even for the simplest multielectron atom, helium, new DI mechanisms are still being found. To first order in the field strength, a strong, external field doubly-ionizes the electrons in helium such that they are ejected into the same direction (front-to-back motion). The ejection into opposite directions (back-to-back motion) cannot be described to first order, making it a challenging target for control. Here, we address this challenge and optimize the field with the objective of back-to-back double ionization, using a (1+1)-dimensional model. The optimization is performed using four different control procedures: (1) short-time control, (2) derivative-free optimization of basis expansions of the field, (3) the Krotov method and (4) control of the classical equations of motion. All four procedures lead to fields with dominant back-to-back motion. All the fields obtained exploit essentially the same two-step mechanism leading to back-to-back motion: first, the electrons are displaced by the field into the *same* direction. Second, after the field turns off, the nuclear attraction and the electron-electron repulsion combine to generate the final motion into *opposite* directions for each electron. By performing quasi-classical calculations, we confirm that this mechanism is essentially classical.

Keywords: double ionization, optimal control, local control, helium, strong-field physics, quantum dynamics

I. INTRODUCTION

Helium, despite its simplicity, can show rich, correlated dynamics of its electrons.^{1–5} One interesting process that appears in strong laser fields is double ionization (DI).^{1,6,7} Besides its fundamental importance for understanding light-matter interactions, double ionization provides new challenges for resolving and controlling attosecond-timescale dynamics of atoms and molecules.^{8,9} DI can be generated by three main types of mechanisms, direct, sequential, and nonsequential double ionization. In direct ionization, the energy of one photon is sufficient to ionize both electrons directly. In sequential ionization, one photon ionizes the first electron and a second photon ionizes the remaining electron. This requires a high photon energy (larger than the second ionization potential, $I_2 = 54.4$ eV for helium¹⁰) or an intensity large enough for over-the-barrier ionization. When the energy of the photon is smaller than the second ionization potential, nonsequential double ionization can occur. This requires an interaction with several photons quasi-simultaneously. The simultaneous motion of the electrons in nonsequential double ionization provides a rich physics with many different mechanisms in various regimes of field intensities and energies, ranging from infrared (IR) to extreme ultraviolet (XUV).^{1,6,7}

One central feature of double ionization is the final relative motion of the electrons. For a linearly polar-

ized field, are they accelerated to the same or to opposite directions?^{2,11–21} The motion into the same direction is called front-to-back or correlated motion whereas the motion into opposite directions is called back-to-back or anti-correlated motion.^{2,11,13,22–24} The external field couples directly only to the front-to-back motion. Hence, to first order, the field can accelerate both electrons simultaneously only in the same direction. In many situations, front-to-back motion is the dominant contribution to double ionization.^{22,25–27} However, in certain regimes such as the two-photon nonsequential double ionization regime (photon energy above 39.5 eV) back-to-back motion is dominant.^{13–15,28,29} Hence, the interplay between the electron-electron, electron-nuclear and electron-field interactions are nontrivial and lead to many different types of mechanisms and effects, including surprising transitions from front-to-back to back-to-back motion, depending on the field parameters.^{1,16,17}

The rich physics of nonsequential double ionization even in the simplest system of the helium atom makes this process interesting and challenging for quantum control optimization. One of the central aims of quantum control theory is to maximize observables of a wavefunction by steering it from an initial state via a time-dependent perturbation to a final state. Typically, the perturbation is an external electromagnetic field interacting with the dipole moment and the initial state is the ground-state. The field is modified until the observable at the final time reaches an optimum. By using different types of algorithms for optimizing the field and by constraining the field to certain shapes or intensities, new insights can be gained and new physical mechanisms can be discovered.^{30–38} While there is an extensive amount

^{a)}Electronic mail: [larsson \[at\] caltech.edu](mailto:larsson@caltech.edu); Present address: Division of Chemistry and Chemical Engineering, California Institute of Technology, Pasadena, CA 91125, USA

of work on controlling laser-matter interactions via selected field parameters such as carrier envelope phase or polarization, so far the application of full control theory to strong-field science and to double ionization in particular has been limited. Some selected applications to date include control of single ionization,^{34,39–41} and experimental pulse optimization for double ionization with IR pulses.³⁷

The objective of this article is twofold. The first objective is to introduce optimal control algorithms to double ionization dynamics and to compare different control procedures. The second objective, as an initial example, is to control back-to-back double ionization by an external field. As we will show, due to the necessity of higher-order effects and many-body contributions, this objective is difficult to achieve and requires a careful choice of the objective to be optimized. In passing, we note that this objective bears a resemblance to controlling the three-body dissociation of an aligned triatomic molecule along the symmetric or anti-symmetric stretch motion.

We use four different control procedures: (1) short-time control, where the control objective is maximized at each time step, (2) derivative-free optimization using a basis representation of the field, (3) the Krotov algorithm and (4) control of the classical equations of motions. We show that a fifth procedure, local control, is not appropriate for our objective but its analysis helps in understanding the interplay between the field and the objective.

All four algorithms used have different strengths and weaknesses and lead to different optimized fields. However, we show below that for this system, all obtained fields lead to the same mechanism: a two-step procedure, where the initial wavepacket is first displaced by the field in the front-to-back direction and then propagated field-free toward the desired back-to-back direction. This mechanism is confirmed by quasi-classical calculations. Thus, the essentials of the mechanism are classical.

Optimal control algorithms typically require tens or hundreds of wavepacket propagations with external fields. This and the computational demands of double ionization in general (a two-particle continuum needs to be adequately described) limits us here to use a (1+1)-dimensional model of the helium atom. This reduced dimensional model can, however, capture the main physics of the full (3+3)-dimensional system.^{19,25,26,42–44} Although we do not predetermine particular pulse shapes and intensities for the control, to reduce overall computational cost we restrict the field duration to a maximal 1.45 fs, which clearly limits the fields to be in the XUV (and X-ray) and few-cycle IR regimes.^{20,45} Aside from these restrictions, the field can take any possible shape and intensity required to reach the objective. While the fields obtained by such a procedure may not be directly experimentally accessible, we extract the mechanism by which the field leads to the desired objective. The key characteristics of the field, e.g. asymmetry of the pulse and intensity patterns, should then be able to be imple-

mented experimentally. The required intensities, pulse durations, and pulse energies we found should be within reach of current Free Electron Lasers.^{13,14,46–48}

Note that although the model is of reduced dimensionality, it is extremely challenging computationally. The many long propagations required for the control methods used here were possible because of an efficient new implementation of the wavepacket dynamics.^{49–52}

The outline is as follows. [Section II](#) introduces the model system and the coordinates used. [Section III](#) defines the regions corresponding to mutually exclusive ionization outcomes and introduces the objectives to be optimized. The various control methods used are presented in [Section IV](#). The results are presented in [Section V](#) and discussed in [Section VI](#). We conclude in [Section VII](#).

II. MODEL SYSTEM

In the following, we use the standard regularized (1+1)-dimensional model of helium, where the quantum mechanical Hamiltonian takes the form of⁵³

$$\hat{H} = \hat{H}_0 + \hat{X}A(t), \quad (1)$$

$$\hat{H}_0 = -\frac{1}{2} \frac{\partial^2}{\partial x_1^2} - \frac{1}{2} \frac{\partial^2}{\partial x_2^2} + V(x_1, x_2), \quad (2)$$

$$V(x_1, x_2) = \sum_{i \in \{1,2\}} -\frac{2}{\sqrt{x_i^2 + \alpha^2}} + \frac{1}{\sqrt{(x_1 - x_2)^2 + \alpha^2}}, \quad (3)$$

$$\hat{X} = -i \left(\frac{\partial}{\partial x_1} + \frac{\partial}{\partial x_2} \right), \quad (4)$$

where x_i is the coordinate of electron i . The regularization parameter α is taken from Ref. 54 and set to 0.739707902. This regularization leads to a match of the exact ground state energy of the helium atom. The interaction with the external field is described by the vector potential $A(t)$ and the interaction operator \hat{X} in (reduced) velocity gauge. An additional term, $A^2(t)/2$, in the Hamiltonian has been eliminated by a standard gauge transformation,⁵⁵ which does not affect the expectation values of interest discussed here. We prefer velocity gauge over length gauge because only fields $E(t) = -dA(t)/dt$ with vanishing time integral are physical.⁵⁶ This can easily be achieved by requiring that the potential $A(t)$ vanishes for $t \rightarrow \pm\infty$. Additionally, the velocity gauge typically is computationally more efficient, especially at higher pulse intensity,⁵⁷ and the local control expressions shown in [Section IV A](#) are simpler in velocity gauge.

To take the fermionic nature of the electrons into account, we write the total wavefunction as direct product of a spin-dependent and a coordinate-dependent part. Since the non-relativistic Hamiltonian does not couple different spins, the spin-dependent part of the wavefunction remains constant during the time evolution. For helium, the electronic ground state is a singlet state whose

spin-dependent part is antisymmetric with respect to exchange of the electrons, $2^{-1/2}[|\alpha_1\beta_2\rangle - |\beta_2\alpha_1\rangle]$. Thus, to ensure total antisymmetry of the wavefunction with respect to exchange of the electrons, the *coordinate*-dependent part of the wavefunction has to be *symmetric*, $\psi(x_1, x_2) \stackrel{!}{=} \psi(x_2, x_1)$. Symmetry can be exploited by rotating the coordinate system by 45° . In this rotated coordinate system, the coordinates u and v are defined as

$$u = \frac{x_1 + x_2}{2}, \quad v = \frac{x_1 - x_2}{2}, \quad (5)$$

$$\Leftrightarrow u + v = x_1, \quad u - v = x_2. \quad (6)$$

Exchange of x_1 and x_2 leads to a sign flip in v . Accordingly, the wavefunction is axially symmetric in v ,

$$\psi(u, v) = \psi(u, -v). \quad (7)$$

We will exploit this symmetry by using only symmetric basis functions in the v coordinate, thus decreasing the number of required basis functions by two, compared to the unrotated coordinate system; see Section A in the supplementary material.

Besides exploiting symmetry, this coordinate system allows for a very simple interpretation of the wavefunction in terms of the relative motion of the electrons; see Fig. 1. Comparing the electronic motion in u and v with the vibrational normal modes of a diatomic system, v describes a symmetric stretch mode and u describes an anti-symmetric stretch mode. Large values of v (compared to u) indicate large separations of the two electrons: They are on different sides of the nucleus. In contrast, large values of u (compared to v) indicate that they are on the same side of the nucleus and that they approach each other with decreasing v .

Inserting Eqs. (6) into Eqs. (2) and (4) leads to the definitions of the field-free Hamiltonian and the field-interaction operator in this rotated coordinate system:

$$\hat{H}_0 = -\frac{1}{4} \left(\frac{\partial^2}{\partial u^2} + \frac{\partial^2}{\partial v^2} \right) + V(u, v), \quad (8)$$

$$V(u, v) = \frac{1}{\sqrt{(2v)^2 + \alpha^2}} - \frac{2}{\sqrt{(u+v)^2 + \alpha^2}} - \frac{2}{\sqrt{(u-v)^2 + \alpha^2}}, \quad (9)$$

$$\hat{X} = -i \frac{\partial}{\partial u}. \quad (10)$$

The potential $V(u, v)$ is shown in Fig. 2. Note that the repulsive electron-electron interaction is peaked along the $v = 0$ line and the attractive electron-nuclear interaction is peaked along the diagonal $u = v$ lines.

III. REGIONS OF IONIZATION

In the continuum, there are three regions with different characteristics. They are shown schematically in Fig. 1.

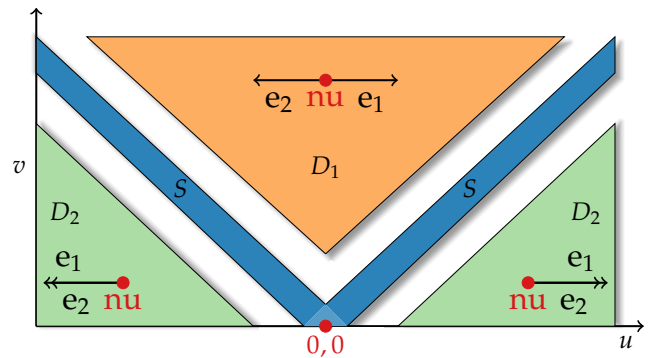


FIG. 1. Regions of the one-dimensional helium atom in the continuum for the rotated coordinate system [Eq. (5)]. The red dot marks the origin where the ground-state density is peaked. The blue region S corresponds to single ionization and the two regions $D_{\{1,2\}}$ denote double ionization and are not connected. D_1 (D_2) corresponds to double ionization where the electrons are ionized into opposite (same) directions. The motions of the two electrons are depicted by the small diagrams; showing the nucleus as a red dot. The white region in between denotes an intermediate between single and double ionization. The regions are only shown for values of v larger or equal to zero. For negative values, the schematic is mirrored; compare with Fig. 2.

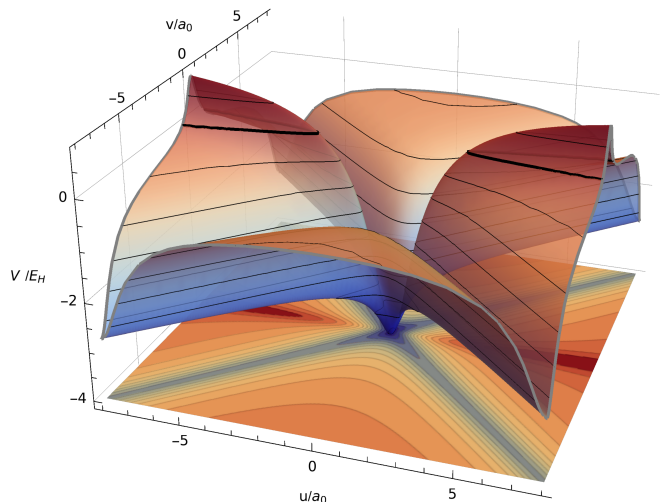


FIG. 2. Potential $V(u, v)$ [Eq. (9)] of the helium model in the rotated coordinate system [Eq. (5)]. The contour line at $V(u, v) = 0$ is highlighted by thicker lines, and parts of the potential are plotted transparently in order to recognize the part at $v > 0$. Note the axial and mirror symmetry of the potential, $V(u, v) = V(u, -v) = V(-u, v) = V(-u, -v)$.

S corresponds to single ionization. D_1 (D_2) corresponds to double ionization where the electrons are ionized into different (same) directions. When double ionization to either D_1 or D_2 occurs, typically parts of the wavefunction remain in the single ionization region S .

The field interaction operator \hat{X} in the rotated coordinate system, Eq. (10), reveals that an external field couples only with the u direction. That is, both electrons

are accelerated into the same direction. If the perturbation induced by the external field is stronger than the Coulomb repulsion of the electrons, they mainly occupy region D_2 , indicating a correlated, or front-to-back process of the double ionization. An anticorrelated, back-to-back process is apparent if the electrons occupy region D_1 . Typically,^{25,26} both regions D_2 and D_1 are occupied but, due to the form of the perturbation induced by the field, there is a substantially larger fraction of the wavepacket in region D_2 .⁵⁸

Here, our goal is to reverse this situation and to increase the occupancy of region D_1 , compared to region D_2 . The optimal choice of target would be a wavepacket that is doubly ionized with large v but centered along $u = 0$. Since the external laser field couples only with the u direction, this can be achieved solely by an interplay between the external field and the Coulomb repulsion of the electrons.

IV. CONTROL METHODS

The goal of quantum control theory is to steer *via* an external electromagnetic field (or potential) $A(t)$ the evolution of the wavefunction $|\psi(t)\rangle$. The evolution is determined by the time-dependent Schrödinger equation (TDSE)

$$i\frac{\partial}{\partial t}|\psi(t)\rangle = \hat{H}|\psi(t)\rangle \quad (11)$$

$$= \hat{H}_0|\psi(t)\rangle + \hat{X}A(t)|\psi(t)\rangle, \quad A(t) \in \mathbb{C}, \quad (12)$$

where \hat{H}_0 is the field-free Hamiltonian and \hat{X} the (typically electromagnetic) interaction operator, which is multiplied with the field $A(t)$. In control theory, the field is treated as a parameter in order to optimize for a specific goal.

A wide variety of optimization goals can be formulated in terms of a control functional J that solely depends on the wavefunction at final time T . It takes the form of

$$J = \langle \psi(T) | \hat{O} | \psi(T) \rangle, \quad (13)$$

which should be maximized.^{31,59–61} \hat{O} is Hermitian and either some operator whose expectation value at final time T should be optimized, or, more commonly, a projection operator $|\phi\rangle\langle\phi|$ in order to optimize for a particular state $|\phi\rangle$. As explained in Section II, the operator \hat{O} should be chosen in such a way that maximizing J corresponds to the major contribution of the wavefunction coming from region D_1 . For example, this can be achieved either by choosing \hat{O} to be the position operator $\hat{O} = v^{62}$, or to be a projector, $\hat{O} = |\phi_v\rangle\langle\phi_v|$, where ϕ_v is a state localized in D_1 . Other choices will be discussed later.

Quantum control theory can be implemented in various ways. We start our analysis with local control theory in Section IV A and show the difficulties of using this

method for our objective. While we do not include results of local control theory in the main text,⁶³ the analysis will be helpful for understanding more about the interplay of the field with our objective and it will help us choosing appropriate gauges and definitions of objectives for the other control algorithms used.

Following that, we present the three different quantum control algorithms that are actually used in the main text, short-time control (Section IV B), derivative-free optimization (Section IV C 1) and the Krotov method (Section IV C 2). Furthermore, we apply optimal control to the classical equations of motions (Section IV D). All methods have advantages and disadvantages and may lead to different pulses and hence different physical mechanisms. However, in this work, we show that *all* four control methods (including the classical control method) lead to essentially the same physical mechanism. This is discussed in Section VI. Note that since the different control methods involve different numerics, the form and choice of target operator (state or projector) may have to be modified depending on the control methodology.

A. Local Control

One way to maximize Eq. (13), that is, some property of the wavefunction at final propagation time, is to maximize this property *during* the time propagation for all *intermediate* times. This is the idea of local control theory. There, the field $A(t)$ at time t_0 is varied *locally* at time t_0 for a small time-interval $t \in [t_0, t_0 + \Delta t]$ in order to optimize the expectation value of some operator \hat{O} .^{31,64} In the following, we will assume that \hat{O} is time-independent. According to Ehrenfest's theorem, the rate of $\langle \hat{O} \rangle$ then becomes

$$\frac{d}{dt}\langle \hat{O} \rangle = i\langle \psi(t) | [\hat{H}_0, \hat{O}] | \psi(t) \rangle + iA(t)\langle \psi(t) | [\hat{X}, \hat{O}] | \psi(t) \rangle, \quad (14)$$

where $[\hat{A}, \hat{B}]$ is the commutator of operators \hat{A} and \hat{B} . Provided that \hat{O} does not commute with the field interaction operator, \hat{X} , the temporal change of $\langle \hat{O} \rangle$ can be controlled by an appropriately chosen $A(t)$.

Eq. (14) can be written as

$$\frac{d\langle \hat{O} \rangle}{dt} \equiv C(t) = \mathcal{Y}(t) + A(t)\mathcal{Z}(t). \quad (15)$$

This equation gives us a means of optimizing $C(t)$ by controlling the field, $A(t)$. As $\mathcal{Z}(t)$ depends on $[\hat{X}, \hat{O}]$, the optimizing expression for $A(t)$ depends on the form of \hat{O} and the form of \hat{X} , the latter depending on the gauge.

In the length gauge, \hat{X} *commutes* with operators that are functions of the coordinates such that no field-dependent expressions are obtained to first order. Although local control is, in principle, possible *via* a second-order expression (see Section B.1 in the supplementary

material), this turns out to be very unstable numerically and is not pursued further.

Instead, we employ the velocity gauge. For reasons that will become clear below, here, we choose some operator \hat{O} instead of a projector for optimization. Assuming that \hat{O} depends only on u and v (and not derivatives of u or v), $\hat{O}(u, v)$, inserting Eqs. (8) and (10) into Eq. (14) yields

$$\begin{aligned} \frac{d\langle O(u, v) \rangle}{dt} = & -\frac{i}{4} [2\langle O_v(u, v) \partial_v \rangle + \langle O_{vv}(u, v) \rangle \\ & + 2\langle O_u(u, v) \partial_u \rangle + \langle O_{uu}(u, v) \rangle] \\ & + A(t) \langle O_u(u, v) \rangle, \end{aligned} \quad (16)$$

where $O_{uu}(u, v) = \frac{\partial^2 O(u, v)}{\partial u^2} \equiv \partial_u^2 O(u, v)$ and so on. As noted in Section II, the field couples only with the u direction. This is evident from the form of Eq. (16), where $A(t)$ couples solely with $\langle O_u(u, v) \rangle$, which needs to be non-vanishing for controlling $\langle \hat{O} \rangle$. Hence, product forms such as $\hat{O}(u, v) = \tilde{O}(u) \cdot \tilde{O}(v)$ or non-separable functional expressions for $\hat{O}(u, v)$ are required, and there must be a dependence of \hat{O} on u .

Besides the necessity to use non-separable forms, in order to steer the wavefunction into region D_1 the operator $\hat{O}(u, v)$ also needs to have reasonable overlap with the origin where the ground state, $|\psi(0)\rangle$, is localized. This is the reason why for the local control procedure \hat{O} should be an operator and not a projector of a final state located solely in D_1 .

Comparing Eq. (16) with Eq. (15) reveals that $\mathcal{Y}(t)$ is nonzero. This is in contrast to previous applications of local control theory, where \hat{O} commuted with \hat{H}_0 , resulting in vanishing $\mathcal{Y}(t)$.^{64,65} In that case, Eq. (15) takes a particularly simple form and $\langle \hat{O} \rangle$ is maximized by setting $A(t)$ to the complex conjugate of $\mathcal{Z}(t)$. Here, this procedure does not work. An attempt to find an expression by enforcing $C(t)$ to have a predetermined functional form is shown in Section B.1 in the supplementary material. However, we observed numerical difficulties with this approach, leading to very jagged pulses that do not maximize $\langle \hat{O} \rangle$ at all time steps. In principle, control via $\frac{d^2 \langle O(u, v) \rangle}{dt^2}$ is possible but the explicit dependence of $\frac{d^2 \langle O(u, v) \rangle}{dt^2}$ on $A^2(t)$ and $\frac{dA(t)}{dt}$ also leads to numerical difficulties.

Due to the numerical difficulties of using local control for our objective, we do not include the results of this procedure in the main text, but in the supplementary material.⁶⁶ However, its analysis gained insights into the optimal choice of gauge and the form of \hat{O} .

B. Short-time control

As alternative to local control, we use a short-time control optimization. Specifically, $|\psi(t + \Delta t)\rangle$ is evaluated explicitly and the new $A(t + \Delta t/2)$ is optimized numer-

ically (a one-dimensional maximization problem), without the need for analytical formulae for time-derivatives. More details on the procedure are presented in Section B.2 in the supplementary material. Strictly speaking, for a given time step Δt , the short-time control algorithm includes higher-order effects. As will be apparent below, this leads to a loss of the local control property of a monotonically increasing objective. However, in the limit of $\Delta t \rightarrow 0$, the standard local control expression can be obtained (and with it the associated numerical difficulties, as discussed above).

C. Global Control

An alternative to local quantum control is *global* optimization procedures that maximize the final state or an expectation value by varying the parameters of the field simultaneously at all times⁶⁷. In contrast to local control, this means that the target expression need not monotonically increase during all propagation times.⁶⁴ Instead, the target can be chosen to depend only on the state at final propagation time. This relaxes the constraints that local control puts on the optimization procedure such that other fields and other physical processes may be found. Compared to local control methods, global control methods are typically much more resource-intensive as they require an iterative approach where the TDSE is solved many times until the optimal field is found, whereas local control procedures require only one time propagation.

Global control can be implemented in different ways, two of which will be presented in the following.

1. Derivative-free optimization

A simple scheme for global control optimization is to represent the field in terms of N_g functions g_i and to optimize the (possibly nonlinear) parameters,

$$A(t) \approx \sum_{i=1}^{N_g} g_i(t; \vec{p}_i). \quad (17)$$

The advantage (and disadvantage) of this approach is that the form of the field is predetermined by the form of g_i . With that, the spectral bandwidth can be limited or a particular pulse shape (e.g., Gaussian for $N_g = 1$) can be required. This, however, results in a constrained optimization of $A(t)$, making the optimization procedure often more difficult.

For finding optimal parameters \vec{p}_i , in principle, the gradient of J with respect to the parameters can be derived using the approach from the next Section IV C 2. However, especially for nonlinear optimizations, the gradient can be noisy. This renders standard gradient-based optimization algorithms useless. Instead, black-box derivative-free optimization algorithms are typically used.⁶⁸ These can be either heuristic algorithms that

search for global minima of the optimization landscapes (like genetic algorithms) or algorithms for finding local minima by estimating the gradient numerically. Both types of algorithms will be used in this work.

Due to the more numerical nature of the derivative-free optimization, the objective does not need to be of the particular form shown in Eq. (13). Instead, *any* objective can be chosen. Here, we chose to maximize the overlap with two states:

$$J = |\langle \psi(T) | \phi_1 \rangle - w_2 \langle \psi(T) | \phi_2 \rangle|, \quad (18)$$

where w_2 is a weight. The states $|\phi_i\rangle$ can take *any* form and do not even need to be square integrable. The overlap of $|\psi(T)\rangle$ with $|\phi_1\rangle$ is maximized. Hence, $|\phi_1\rangle$ should be located in region D_1 (compare with Fig. 1). In contrast, the overlap of $|\psi(T)\rangle$ with $|\phi_2\rangle$ is minimized. Hence, $|\phi_2\rangle$ should be located in region D_2 . Furthermore, for the electrons to move into opposite directions, there should be no momentum in u but a positive momentum in v , giving an additional property $|\phi_i\rangle$ should fulfill.

2. Krotov method

Another approach to global quantum control takes derivative information into account. This is performed within a variational framework where $A(t)$ is discretized, leading to a very robust and general approach. However, adding particular constraints to the field is difficult (see Refs. 69,70 for some approaches) and some target operators \hat{O} may lead to numerical instabilities due to the lack of constraints (i.e., very large values of $A(t)$ or many oscillations). \hat{O} thus needs to be well-chosen.

To obtain the optimized field in discretized time, we use the Krotov method.^{71–73} Therein, not only J but the following functional is optimized:

$$\bar{J} = J + J_1 + J_2 + J_3, \quad (19)$$

with

$$J = \langle \psi(T) | \hat{O} | \psi(T) \rangle, \quad (20)$$

$$J_1 = -2\Re \int_0^T \langle \chi(t) | \partial \psi(t) / \partial t \rangle dt, \quad (21)$$

$$J_2 = +2\Re \int_0^T \langle \chi(t) | [\hat{H}_0 + \hat{X} A(t)] | \psi(t) \rangle dt, \quad (22)$$

$$J_3 = - \int_0^T \lambda(t) [A(t) - A^{\text{ref}}(t)]^2 dt. \quad (23)$$

Here, $\langle \chi(t) |$ is a Lagrange multiplier or dual function. The functional J_3 restrains the fluence of the field. The smaller the $\lambda(t)$, the smaller the contribution of J_3 to \bar{J} and hence the larger the allowed deviations from the reference field A^{ref} .

After discretization in t , this optimization problem finally yields the following update of the field at iteration

p at time t :

$$A^{(p)}(t) = A^{\text{ref}}(t) + \frac{1}{\lambda(t)} \Im \left\langle \chi^{(p-1)}(t) \left| \hat{X} \right| \psi^{(p)}(t - \Delta t) \right\rangle. \quad (24)$$

In the Krotov algorithm, the dual state $|\chi(T)\rangle$ at final propagation time T is obtained by applying \hat{O} on $|\psi(T)\rangle$. The dual state is then propagated backward in time. The new wavefunction $|\psi(t)\rangle$ and the new values of the field are then obtained by a forward propagation using Eq. (24). This procedure is repeated until convergence.

Provided that \hat{O} is a positive semidefinite operator, e.g., a projector, it can be shown that Krotov's method gives monotonic convergence with respect to \bar{J} . However, it may happen that only J_3 in \bar{J} is optimized and not the actual target J . This can be avoided by setting the reference field A^{ref} to the field of the previous iteration, $A^{(p-1)}$. Then, the method is monotonically convergent both with respect to \bar{J} and J .⁷³

The objective in the Krotov optimization can be an expectation value or a particular state (using a projection operator as \hat{O}). It is not immediately clear which choice will lead to a better result. Numerically, we found that optimizing for an expectation value is much easier. The major reason is that, when optimizing for a particular state, the Krotov optimization is very sensitive to the functional form of the state. Since the target state will actually be used for the backpropagation, it is very important that the target state is physical and can be reached with a reasonable pulse shape. This is different from derivative-free optimization where the target state does not need to be well-behaved.

D. Control of classical dynamics

The previous methods dealt with control algorithms for quantum mechanics. However, optimal control can also be formulated for classical mechanics. Performing both classical and quantum control optimizations on the same systems pinpoints the quantum effects and gives new insights. Practically, the classical equations of motions are, of course, much easier to solve.

For controlling classical mechanics, Hamilton's equations of motion

$$\frac{d\vec{p}}{dt} = -\frac{\partial H}{\partial \vec{x}}, \quad \frac{d\vec{x}}{dt} = \frac{\partial H}{\partial \vec{p}} \quad (25)$$

are solved for the classical Hamiltonian H . For control optimizations, a classical Lagrangian can be formulated similar to the Lagrangian formulation of the Krotov method (Section IV C 2). The equations are then solved on a time grid as in the Krotov method by discretizing the equations of motions using, e.g., the fourth-order Runge-Kutta propagator.⁷⁴ The control procedure can then be performed using standard black-box software.⁷⁵

V. RESULTS

We now present the outcome of the various control methods. To solve the time-dependent Schrödinger equation we use the dynamically pruned discrete variable representation (DP-DVR).^{49–51} In the DP-DVR, the direct-product DVR basis is pruned in a non-direct-product fashion at each time step. This allows for a very efficient representation of the wavepacket at all propagation times. We found it faster than FFT-based dynamics, even when the latter is performed on a general purpose graphical processing unit (GPGPU). More details are presented in Section A of the supplementary material.

It will be shown later in Section VI that, despite the superficial differences of the optimized pulses, they all share common characteristics and they all result in the same physical mechanism, namely a two-step procedure where the wavefunction is first displaced in u and then evolves into region D_1 .

We further note that we have tested many different operators and show here only those choices that lead to the most satisfying results. This explains why we sometimes use slightly different functional forms of the operator for the different control methods. However, in general, we found that operators that maximize region D_1 in coordinate space are most useful. Operators depending on the expectation values of the momenta have also been tested but were found to be less useful. Further details of the simulation procedures are given in Section B in the supplementary material. Our results from local control theory are not discussed in the main text but in Section C.1 of the supplementary material. Spectrograms of all fields shown are given in Section D of the supplementary material.

A. Short-time control

For the short-time control procedure, we need to specify the form of the operator to be maximized, $\hat{O}(u, v)$. For simplicity, we chose $\hat{O}(u, v) = \tilde{O}(u) \cdot \tilde{O}(v)$. To confine the region to be optimized in u , we used a Gaussian form, $\tilde{O}(u) = N \exp(-\alpha u^2)$, with N being a normalization factor and $\alpha = 2/5$ a.u. To ensure both reasonable overlap around the origin and a steering to larger v values, we chose $\tilde{O}(v) = v^2$.

The result using the short-time control optimization described in Section IV B is presented in Fig. 3. The field obtained is complex and shows many oscillations with jagged features. Notably, $\langle \hat{O} \rangle$ is not monotonically increasing. This is due to a restriction on the maximal field amplitude⁷⁶ and the nature of the short-time optimization process as discussed further in Section VI B. Even though single ionization dominates, there is a clear increase in the objective and there is larger occupancy in region D_1 , compared to region D_2 . The results are discussed further in Section VI.

B. Derivative-free optimization

In the following, we present three different results that differ in particular states $|\phi_i\rangle$ used to define the objective J (smooth triangles based on the tanh function or Gaussians):

$$\phi_{1a}(u, v) = N \exp(-\alpha u^2) \exp[-\alpha(v - v_0)^2 + ip_0(v - v_0)], \quad (26)$$

$$\phi_{1b}(u, v) = 1 - \{\tanh[s \cdot \sin(\pi/4)(a(u) - v + v_0)] + 1\}/2, \quad (27)$$

$$\phi_2(u, v) = \{\tanh[s \cdot \sin(\pi/4)(a(u) - v - v_0)] + 1\}/2, \quad (28)$$

with $a(u)$ being a regularized function for taking the absolute value of u :

$$a(u) = u^2 / \sqrt{u^2 + 0.004}. \quad (29)$$

The objectives are then defined by

$$J_a = \langle \psi(T) | \phi_{1a} \rangle - 10 \cdot \langle \psi(T) | \phi_2 \rangle, \quad (30)$$

$$J_b = \langle \psi(T) | \phi_{1b} \rangle - 1 \cdot \langle \psi(T) | \phi_2 \rangle. \quad (31)$$

Choosing the parameters $\alpha = 2/39$, $p_0 = 3$, $v_0 = 70$ positions the Gaussian $\phi_{1a}(u, v)$ in region D_1 . $\phi_{1b}(u, v)$ is a smooth triangle located in region D_1 with $v_0 = 40$. In addition, $\phi_2(u, v)$ is a smooth double triangle but it is located in region D_2 with $v_0 = 65$ and $s = 0.3$.

For the pulse parametrization, inspired by Refs. 78–80, we chose the real part of a single complex Gaussian with complex width parameter α , which enables chirped fields:

$$g(t) = A_0 \exp[-\Re\alpha(t - t_0)^2] \cos[(t - t_0)(\omega_0 - \Im\alpha(t - t_0))]. \quad (32)$$

It turned out that optimizing one single function is sufficient. The form of Eq. (32) leads to the following five parameters $\{A_0, \Re\alpha, \Im\alpha, \omega_0, t_0\}$ to be optimized.

The choice of objectives and optimization algorithms for the pulses (a)-(c) are as follows. Pulse (a) used J_a in Eq. (30). The other pulses used J_b in Eq. (31). For pulses (b) and (c), A_0 was fixed and not optimized. Pulses (a) and (c) were results of local, derivative-free optimizations *via* the COBYLA⁸¹ and the BOBYQA⁸² algorithms, respectively. The initial guess pulse was arbitrarily chosen to have the parameters $\{A_0, \Re\alpha, \Im\alpha, \omega_0, t_0\} \sim \{2.3, 0.07, -0.17, 10.8, 5.9\}$, and does not lead to the desired objective. Pulse (b) was a result of global optimization *via* the differential evolution algorithm.⁸³ See Section B.3 in the supplementary material for further details. We note that the results we present here may not be “optimal” compared with other results using the same optimization algorithm. Instead, we chose those fields that led to a simple pulse shape and had a clear visual appearance of our control aim (major part of the wavefunction in region D_1).

The three obtained pulses and the wavefunction at the end of the propagation time are shown in Fig. 4. Since

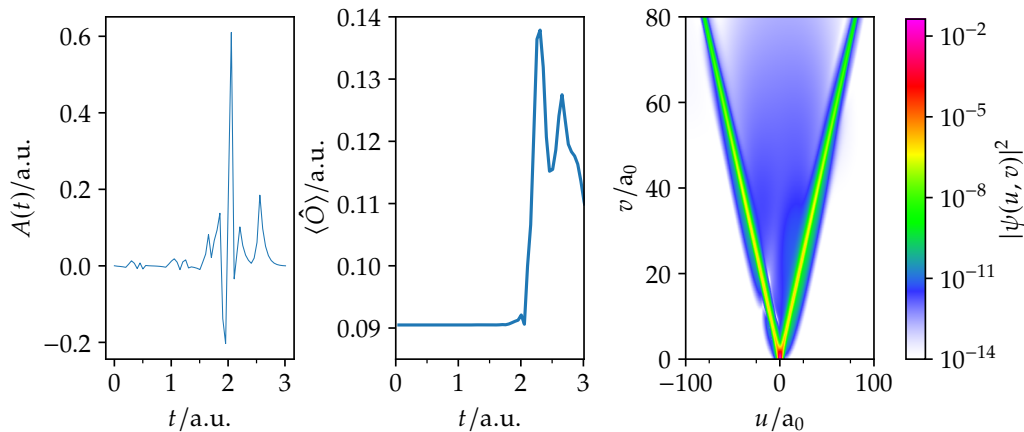


FIG. 3. Short-time control optimization. The left panel shows the optimized pulse, the middle panel shows the expectation value of $\hat{O} = N \exp(-2u^2/5)v^2$ to be optimized, and the right panel shows the square of the wavefunction at the final propagation time $T = 60$ a.u. The short-time control procedure (see Section IV A) is used for the optimization until $t = 3$ a.u. Afterwards, the wavefunction is propagated field-free. The colormap has been taken from Ref. 77.

all fields vanish after $t = 15$ a.u., we show them only until this time. The final propagation time was $T = 60$ a.u.. The parameters for Eq. (32) are stated in Table I. Note that these three pulses are only a selection of a plethora of different pulses, obtained by different algorithms and different targets, but their shapes are characteristic of the other pulses as well.

All pulses shown lead to an increase of the wavefunction in region D_1 , compared to region D_2 , such that they fulfill the requested task.

TABLE I. Derivative-free optimization. Rounded values of the optimized parameters for the pulses depicted in Fig. 4. The form of the pulse is given by Eq. (32). Atomic units are used unless stated otherwise.

pulse	A_0	$I[\text{W}/\text{cm}^2]$	$\Re\alpha$	$\Im\alpha$	t_0	ω_0	$\omega_0[\text{eV}]$
(a)	46.6	$8 \cdot 10^{19}$	0.13	-0.15	7	5.90	160
(b)	-4.43	$7 \cdot 10^{17}$	12	0.74	2	1.43	38.8
(c)	-4.43	$7 \cdot 10^{17}$	0.24	-0.85	5	2.19	59.3

C. Krotov

For the Krotov algorithm, we tried both projection operators (optimizing for a particular state) and general operators (optimizing for expectation values) as optimization targets \hat{O} . Using a projection operator led to no satisfying results. More details are given in Section C.2 in the supplementary material.

Here, we present only results for optimizing expectation values of some operator \hat{O}^K . We closely follow the procedure used in Section VB but used the functional forms of ϕ_i as expectation values. In particular, we used the form of two smooth triangles, Eq. (27) and (28), from Section VB with shift v_0 set to 40. That is,

$$\hat{O}^K(u, v) = \phi_{1b}(u, v) - \phi_2(u, v).$$

Fig. 5 shows the final field from the Krotov iteration. Clearly, region D_1 is more occupied than region D_2 .

D. Control of classical dynamics

Controlling the classical dynamics turned out to be much easier and various objectives gave very similar results. As classical dynamics is much simpler, even for complicated control problems, we chose a more complicated objective J_C that contains a time-dependent term, namely

$$J_C = -\eta v(T)p_v(T) + \int dt [u(t) \tanh(\xi t)]^2 \quad (33)$$

with parameters $\eta = 100$ and $\xi = 0.1$. The time-dependent term in J_C ensures that large values of $|u|$ occur only during the propagation but not at the end. In v , we maximized both the coordinate and the momentum such that the trajectory ends the simulation with an appropriate direction. The obtained classical trajectory in (u, v) and the optimized field are shown in Fig. 6.

VI. TWO-STEP MECHANISM

We will now discuss the wavefunction propagation that takes place for each field and detail the resulting physical mechanism. It will turn out that all pulses share common characteristics and that they all lead to essentially the same physical mechanism.

For a more thorough analysis, both the wavepacket in coordinate space and its reduced densities in phase space are shown for selected times. For the phase-space analysis, the Husimi Q representation is used, that is, a

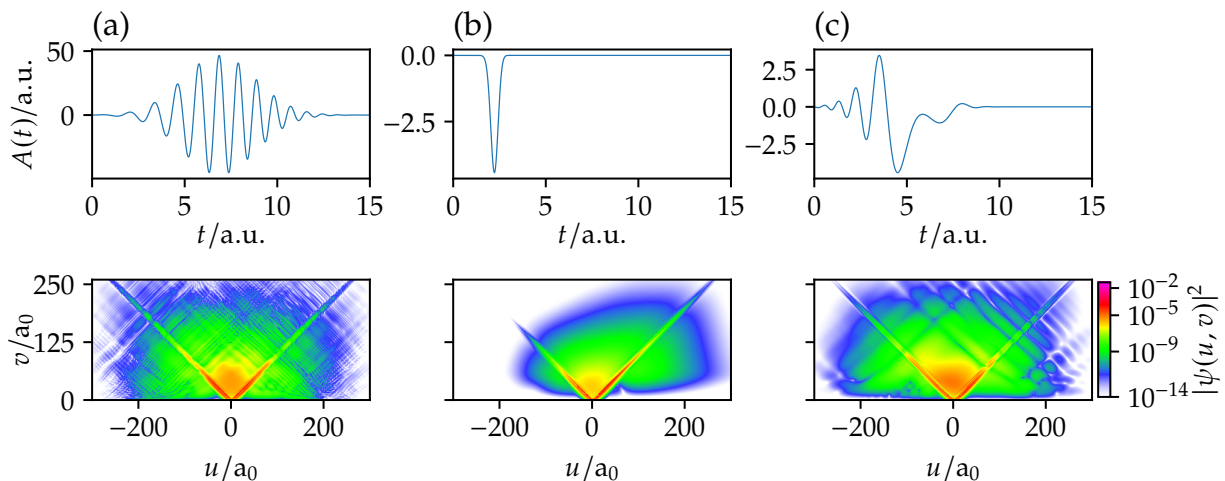


FIG. 4. Derivative-free optimization. The pulse with parameters to be optimized is shown in Eq. (32). The left panels (a) show the COBYLA-optimized pulse (local optimization) using the objectives described at Eq. (26) and Eq. (28). The middle panels (b) show the pulse optimized *via* differential evolution (global optimization), where the objective of Eq. (26) is replaced by Eq. (27). The right panels (c) show the BOBYQA-optimized pulse (local optimization) (same objective as (b)). The top panels show the optimized pulses. For $t > 15$ a.u., all pulses have vanishing values. See Table I for the pulse parameters. The lower panels show the square of the wavefunction at the final propagation time $T = 60$ a.u.

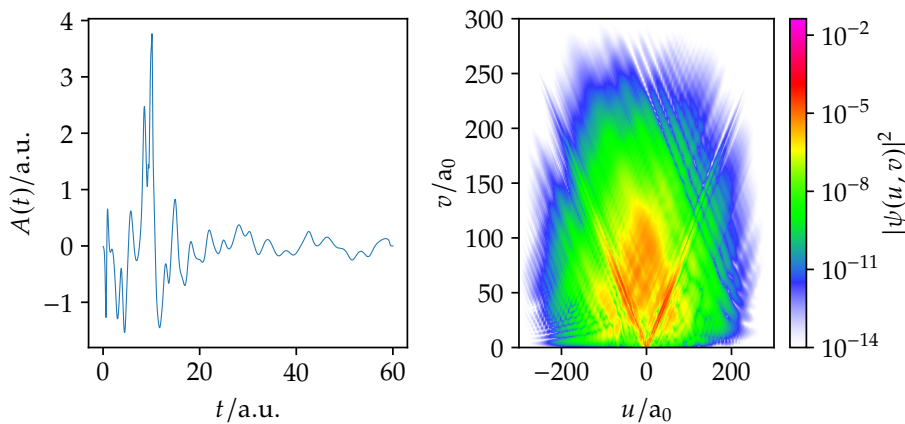


FIG. 5. Krotov optimization. The expectation value of Equations (27) and (28) is optimized (same as in the derivative-free optimization but with a different shift $v_0 = 40$; compare with pulses (b) and (c) in Fig. 4). The left panel shows the optimized pulse. The right panel shows the square of the wavefunction at the final propagation time $T = 60$ a.u.

projection of the state onto coherent states:⁸⁴

$$Q(x, p) = \frac{1}{\pi} |\langle g_{x,p} | \psi \rangle|^2, \quad (34)$$

$$g_{x_0, p_0}(x, p) = \left(\frac{2\alpha}{\pi} \right)^{\frac{1}{4}} \exp \left[-\alpha(x - x_0)^2 + i \frac{p_0}{\hbar} (x - x_0) \right] \quad (35)$$

Essentially, the Husimi Q representation is a continuous version of the “pixelated” von Neumann representation,^{51,85} which we have previously used in similar studies.^{54,86,87} Here, the width parameter α is set to $1/2$, resulting in the same widths in x and p . A phase-space analysis, using Wigner’s representation, has also been performed for double ionization by Lein *et al.* but only

for the u coordinate, focusing on the front-to-back motion of double ionization (same direction of ionization for both electrons).²⁶

For the following discussion, recall that large (small) u values with small (large) v values means that both electrons are on the same (opposite) side of the nucleus; compare with Fig. 1.

We start this section with the results from the derivative-free optimization instead of the results from short-time control. The changed order is due to the fact that the outcomes from the derivative-free optimization have the simplest shapes and thus highlight the main characteristics of all the pulses found. They will also highlight the main physical mechanism that takes place.

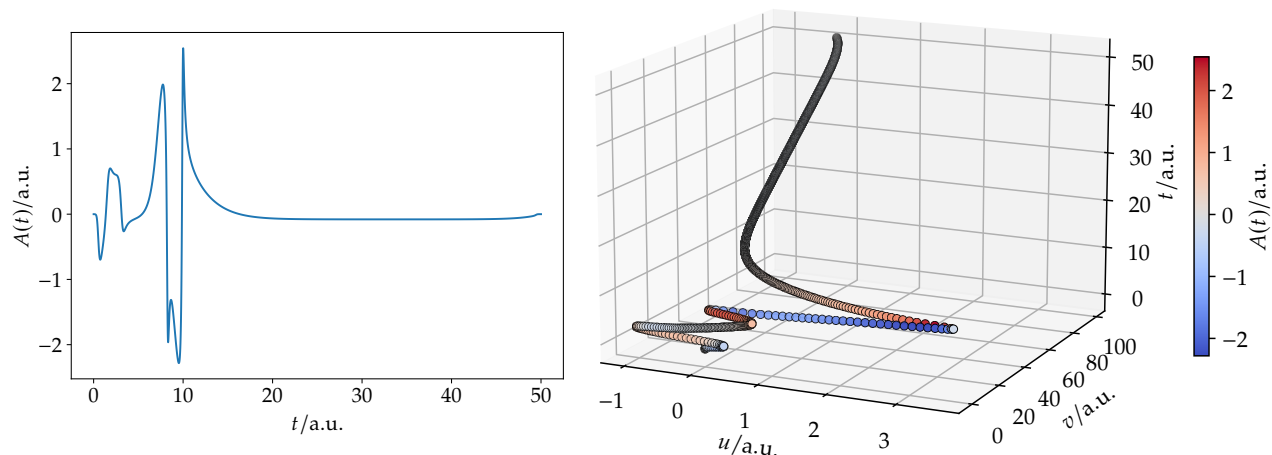


FIG. 6. Classical optimal control result. The objective is shown in Eq. (33). The left panel shows the optimized pulse. The right panel shows the trajectory in u and v as a function of time t (z -axis). The color corresponds to the values of the field.

A. Derivative-free optimization

We first consider the simplest pulse found in our study, namely field (b) obtained from the derivative-free optimization; see Fig. 4. This field consists of just a single pronounced peak at negative values.⁸⁸ The pronounced peak leads to an acceleration of the wavepacket in the u direction. Since the final wavepacket is localized mainly in regions S and D_1 (small u values) but *not* in D_2 (large u values), this pulse is, at first sight, counterintuitive. Nevertheless, an analysis of the wavepacket at different propagation time reveals a clear mechanism.

Fig. 7 shows the reduced density of the wavepacket in coordinate space and phase-space representations for selected propagation times. (Plotting the wavepacket in momentum space is not useful because it does not reveal any coordinate-dependent information.) The pulse generates an acceleration of the wavepacket in the u direction which in turn leads to a displacement of the wavepacket in u ; compare t_1 and t_2 (first and second row) in Fig. 7. Some parts of the wavepacket are scattered at the potential valley but the main part of the wavepacket is simply displaced. The acceleration in u is visible in the Husimi Q distribution of that coordinate. Note that the maximum of the wavepacket is still at $v \sim 0$ where the electrons are affected strongly by their Coulomb repulsion. Therefore, once the wavepacket is displaced and the field vanishes, the wavepacket is driven to larger v values to avoid the Coulomb repulsion. Additionally, it is attracted by the nucleus and thus driven to smaller u values. The net result of the motion is diagonal and in the direction of region D_1 . This is evident from t_3 (third row in Fig. 7). At that time, the wavepacket is again centered around $u \sim 0$ with large components at larger v values. Interference phenomena due to the scattering by the potential valley (along the diagonal) are visible. Note how the wavepacket has gained large positive components in momentum p_v for larger v values; as is evident from

the Husimi Q distribution in coordinate v .⁸⁹ The components in p_v are large enough to drive the wavepacket into the continuum along the v direction. The nuclear attraction (the potential valley) hinders the wavepacket from moving to large negative u values. The phase-space distribution in u becomes almost point symmetric. Thus, the total movement is toward large v values; see the last row in Fig. 7.

To show that the displacement of the wavepacket in u is the first step towards the desired occupancy in region D_1 , the propagation of an initially displaced ground state without the appearance of an external field is shown in Fig. 8. As expected, the occupancy in region D_1 is visible after a propagation for a short time (t_2 ; lower row). At that time, there are also major components in region D_2 but the strong asymmetry of the phase-space distribution in v (lower right panel) will drive the wavepacket to larger v values such that the occupancy in D_2 will vanish. This is evident from inspections of the wavepacket at longer propagation times (not shown) and from the evaluation in Section VID. A plot of the field corresponding to pulse (b) and the optimized expectation value of the observable as a function of time, both for the propagation with an external field and for the displaced wavepacket without a field, is shown in Fig. 9. One clearly sees that the displacement first leads to a decrease in the observable and only afterwards is the observable monotonically increasing.

Overall, there is a simple two-step procedure that leads to the increased occupancy in region D_1 . Pictorially, this two-step procedure is summarized in Fig. 10: The wavepacket starts at the origin (position I) and the large values of the pulse in one direction leads to a displacement in u in the first step. Once the field vanishes, the wavepacket is at position II and the repulsion by the electron-electron Coulomb potential and the attraction by the nuclear Coulomb potential leads, in the second step, to a movement to region D_1 (position III).

This two-step procedure requires that the field has a

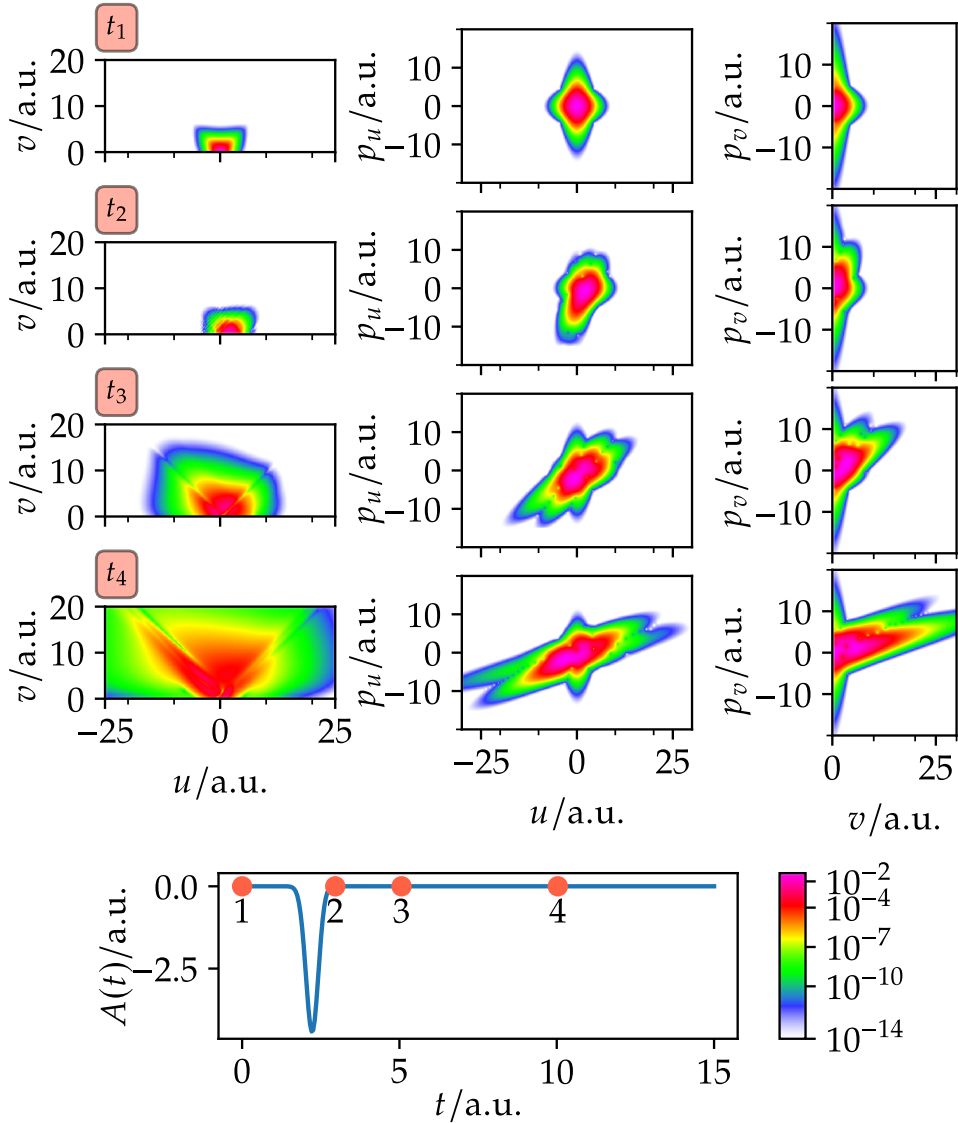


FIG. 7. Analysis of the mechanism of pulse (b) of the derivative-free optimization (Fig. 4). The upper left panels show the square of the wavefunction in coordinate space (u, v) . The upper middle and right panels show the Husimi Q distribution (Eq. (34)) of the reduced densities (wavefunction integrated over the other coordinate) in (u, p_u) (middle panels) or (v, p_v) (right panels), respectively. Each row corresponds to a different time t_i . The lower left panel shows the pulse and the chosen time points t_i .

strong enough amplitude in order to displace the electrons in the u direction for small v values. For these coordinate values, the Coulomb repulsion of the electrons approaches the maximum (see Fig. 2). This requires that the field interaction has to be stronger than the Coulomb repulsion of the electrons. This requirement is similar to that found in textbook discussions of strong-field single ionization, where the magnitude of the field is compared to the Coulomb attraction of the nucleus.

Further tests were performed by scanning the amplitude of the field. An increase in region D_1 is already visible for a field with amplitude of 1 a.u. ($3.5 \cdot 10^{16}$ W cm $^{-2}$). For lower intensities, only single ionization occurs. For amplitudes larger than 10 a.u. ($3.5 \cdot 10^{18}$ W cm $^{-2}$), the dis-

placement is so large that the wavefunction gains enough momentum in u to overcome the nuclear attraction by the Coulomb potential. This leads to an increase in the occupancy in region D_2 .

Although the other fields shown in Fig. 4 look quite different, they actually all follow the same mechanism. For example, field (c) has a large time-asymmetry which implies a similar mechanism; an explicit analysis (not shown here) confirms this. For pulse (a), this is not very clear because there is no evident asymmetry. Indeed, it is the only pulse that has many, “symmetric” cycles (as more standard pulses) but an extremely large amplitude of almost $8.8 \cdot 10^{19}$ W cm $^{-2}$. Reducing the field intensity by a factor of four gives a qualitatively similar result.

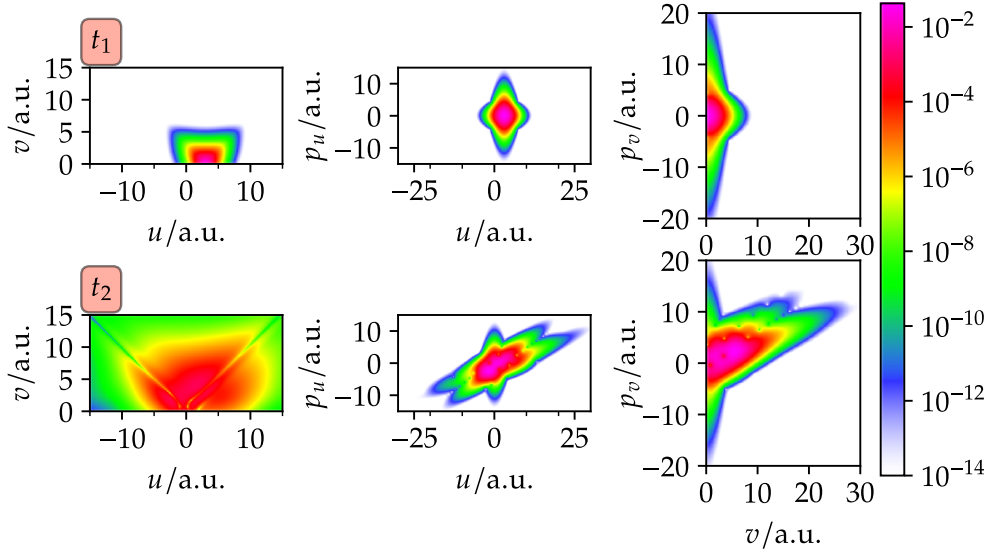


FIG. 8. Same as Fig. 7 but without a field and with an initial wavepacket displaced in u and centered at $u = 3$ a.u. The propagation times are $t_1 = 0$ and $t_2 = 5.02$ a.u.

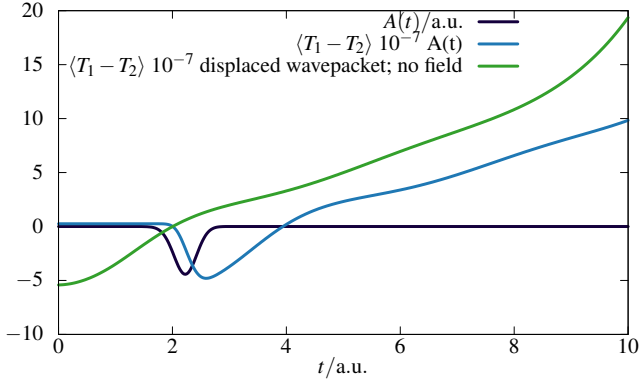


FIG. 9. Field (black curve) and optimized expectation values of pulse (b) of the derivative-free optimization (Fig. 4). The blue (green) curve corresponds to the dynamics presented in Fig. 7 (Fig. 8). The observable is $T_1 - T_2 \equiv \phi_1(u, v) - \phi_2(u, v)$, as defined in Eq. (27) and Eq. (28).

The wavefunctions at different times for that pulse are shown in Fig. 11. The times roughly correspond to different zero-crossings of adjacent half-cycles. At these times, the wavepacket has the maximal displacement. Comparing the wavepacket for subsequent times shows that the center of the wavepacket is moving to larger and larger v values. This is also evident from the Husimi Q distribution in v . The amplitude of the field is large enough that the wavepacket in the u direction is driven mostly by the continuously oscillating field; as a result the Husimi Q distribution in u is almost point symmetric (at a displaced point). Once the field vanishes, the wavepacket has enough positive momentum in v such that the dominant occupancy already created in region D_1 remains.

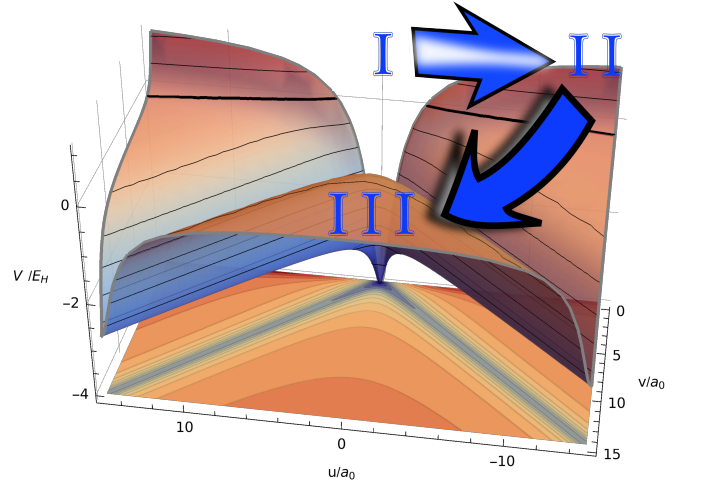


FIG. 10. Schematic of the mechanism of the ionization dynamics analyzed in Figs. 7, 8 and 9. Shown are the potential, the initial (I), intermediate (II) and final (III) locations of the wavepacket. The two-step procedure is shown by the arrows that represent the movement of the wavepacket. Note that the potential is symmetric in v and only non-negative values of v are shown.

The two-step procedure is, essentially, a classical mechanism. Indeed, we are able to confirm this by running quasi-classical trajectories. The starting conditions of the trajectories were obtained by sampling the four-dimensional phase-space Husimi distribution of the quantum mechanical ground state, neglecting zero point energy.^{90,91} Fig. 12 shows the propagation of an ensemble of 10^5 particles with initial displacement in u of 3 a.u. This is the classical counterpart of the quantum mechan-

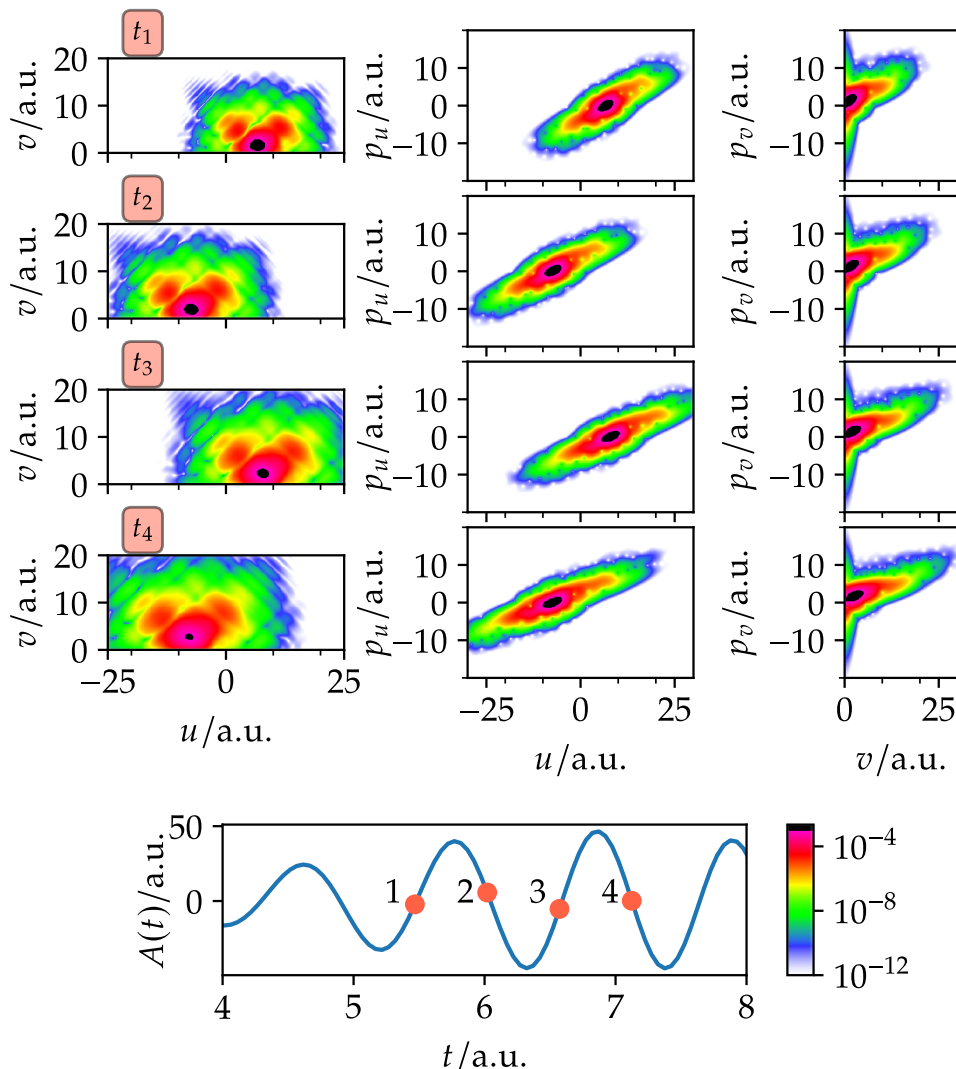


FIG. 11. Same as Fig. 7 but with pulse (a) shown in Fig. 4 (derivative-free optimization). The shown times roughly correspond to the zero-crossings of the 7th to 10th half-cycles.

ical dynamics shown in Fig. 8. Clearly, the final classical phase-space distribution is very similar to that shown in Fig. 8: there is a significant portion of particles in region D_1 and almost no particles in region D_2 . Also the propagation with field (b) (see Fig. 7) leads to a very similar final distribution (not shown here).

B. Short-time control and Krotov optimization

Compared to the parametrized pulses obtained from derivative-free optimizations, the pulses obtained from local control (Fig. 3) and from the Krotov optimization (Fig. 5) are much more complex, making the analysis also more difficult. However, a phase-space analysis reveals that the fields actually by and large lead to the same mechanism. Both fields have a pronounced asymmetry and the mechanism corresponds essentially to the

previously detailed two-step procedure.

The short-time control pulse deserves more attention. In the limit of $\Delta t \rightarrow 0$, the short-time control procedure is the same as the local control procedure. By definition, the local control procedure maximizes the objective at all time steps. This contradicts the two-step mechanism, where the displacement of the wavepacket in u leads to a decrease in the objective. In other words, the local control procedure should not find this mechanism. Here, however, the short-time control procedure with $\Delta t > 0$ differs from local-control as the pulse is *numerically* optimized at each time step. If there is no possible increase in the objective at a given time (subject to a restriction on the maximal field amplitude), the procedure thus finds a field with the smallest possible *decrease* of the objective. With that, the two-step mechanism is possible for the short-time control procedure. Nevertheless, the dominant ionization process of the short-time control

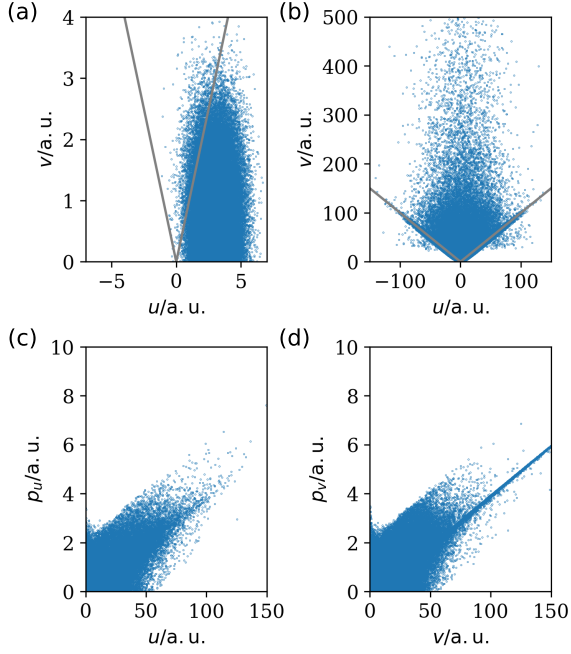


FIG. 12. Quasiclassical trajectories corresponding to the quantum mechanical analogue shown in Fig. 8 (displaced groundstate with field-free propagation). Shown are the initial (panels (a) and (c)) and final ($t = 50$ a.u., panels (b) and (d)) distributions in coordinate (upper panels) and phase space (lower panels). The gray lines along $|u| = v$ in the upper panels should serve as a visual guide. The propagation was performed field-free but the initial starting points were displaced in u by 3 a.u.

pulse is single ionization, indicating that local and short-time control is not an adequate method for our objective. The analysis of local control theory in Section IV A, however, helps in designing appropriate control targets and choosing appropriate gauges.

C. Classical control

The field obtained from classical control also follows, essentially, the two-step procedure. The dynamics was already shown in Fig. 6. The pronounced negative peak at about $t = 9$ a.u. displaces the classical particles to larger u values. Afterward, the particles are driven back to small u and large v values (region D_1). The positive peak for $t > 10$ a.u. increases the displacement in this direction.

A quantum propagation with this field is shown in Fig. 13. Clearly, an occupancy in region D_1 is also obtained here, showing that it is possible in this case to perform solely classical calculations to obtain qualitatively the same mechanism.

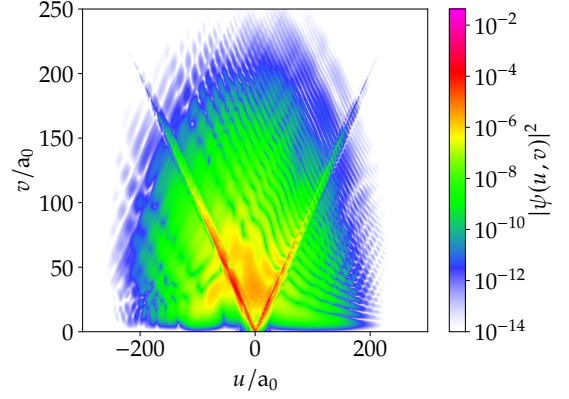


FIG. 13. Quantum wavefunction propagation with field obtained from classical control (compare with Fig. 6). The square of the wavefunction at the final propagation time, $T = 60$ a.u., is shown.

D. Common evaluation

Table II provides a common evaluation of all results with respect to the occupancies in regions D_1 and D_2 at the final propagation time. The occupancies are determined by projectors P^{D_1} and P^{D_2} that project into the two regions of double ionization shown in Fig. 1. The Krotov method exhibits the maximal expectation value $\langle \hat{P}^{D_1} - \hat{P}^{D_2} \rangle$ of 0.283. Field (c) from the derivative-free optimization procedure gives the second largest value (37%, relative to the Krotov result). This is remarkable as this field is much simpler and less intense than that of the Krotov results (compare Fig. 4 with Fig. 5).

Further, for the pulses from the derivative-free optimization procedures, the ratio $\langle \hat{P}^{D_1} \rangle / \langle \hat{P}^{D_2} \rangle$ is around 4 to 6 times larger than that of the Krotov result. That is, the double ionization yield is higher for the Krotov outcome but the ratio of back-to-back motion versus front-to-back motion is higher for the derivative-free optimization outcomes. This is even more extreme for the pulse obtained by the short-time control procedure where double ionization is minimal, but occurs with a strong favor towards back-to-back motion, as is also evident from Fig. 3.

The highest ratio $\langle \hat{P}^{D_1} \rangle / \langle \hat{P}^{D_2} \rangle$ of 403 actually occurs when the ground state is just displaced and evolved field-free afterwards. This shows again that, in our setup, the displacement in u is an essential process that needs to happen for obtaining back-to-back ionization.

We now discuss the validity of our simulation method, namely the nonrelativistic Schrödinger equation within the dipole approximation. Relativistic effects have been shown to be important for field intensities around 10^{20} W/cm².⁹² While field (a) obtained from the derivative-free optimization procedure is in this regime, further tests showed that the mechanism is still valid for smaller intensities up to $3.5 \cdot 10^{18}$ W/cm² (see

TABLE II. Evaluation of the control results by the projectors P^{D_1} and P^{D_2} that project into the two regions of double ionization shown in Fig. 1. Shown are the expectation values of the difference of the projectors P^{D_1} and P^{D_2} , and the ratio of their expectation values for the different fields and control methods. The former (latter) is (in-)dependent on the ionization yield. The projectors are defined similar to the functions $\phi_{1b}(u, v)$ and $\phi_2(u, v)$ from Eq. (27) and Eq. (28), replacing tanh by step functions. The expectation values have been calculated at the final propagation time, $T = 60$ a.u. The range of $\langle \hat{P}^{D_1} - \hat{P}^{D_2} \rangle$ is $[-1, 1]$.

Method	Fig.	Field	$\langle \hat{P}^{D_1} - \hat{P}^{D_2} \rangle$	$\langle \hat{P}^{D_1} \rangle / \langle \hat{P}^{D_2} \rangle$
Short-time Control	3		0.000 000 030	44
Deriv.-Free	4	(a)	0.063	42
		(b)	0.011	65
		(c)	0.10	63
Krotov	5		0.28	9.9
Classical	6, 13		0.015	2.6
Displaced	8		0.035	403

Section VIA). All other fields have intensities below 10^{18} W/cm², where relativistic effects can be neglected. We also tested the validity of the dipole approximation by performing additional simulations that included first and second order corrections to the dipole approximation. While we experienced numerical difficulties in simulating field (a), all other fields, including the Krotov-optimized, showed only minor changes in the wavefunction when simulated beyond the dipole approximation. To summarize, the mechanism and the main characteristics of the fields are neither affected by relativistic effects nor are they affected by the dipole approximation.

VII. CONCLUSIONS

We have investigated the control of double ionization dynamics in a (1+1)-dimensional model of the helium atom for field propagation times up to 1.45 fs. At the onset of ionization, to first order in field strength, an external field can simultaneously accelerate both electrons only into the same direction into the continuum, leading to front-to-back motion of double ionization. Here, the control objective was to obtain a field that does the opposite, namely back-to-back double ionization, where both electrons are ionized into opposite directions. For the propagation times discussed, this can be achieved solely by an interplay between the external field, the electronic repulsion and the nuclear attraction.

We tested four different control procedures. Three of them are based on quantum mechanics whereas the last one uses classical equations of motions: (1) short-time control, where the control objective is maximized locally at each time step; (2) a basis expansion of the field and subsequent derivative-free optimization; (3) the Krotov algorithm, where the field is represented on a time grid and derivative information is taken into account; and (4)

an algorithm based on classical equations of motions and a collocation-based technique that takes derivative information into account.

Furthermore, we analyzed several variations on the local control method and discussed why it is not an appropriate algorithm for our objective. The local control optimization is not appropriate here because (1) the operator whose expectation value is to be optimized does not commute with the field-free Hamiltonian (i.e. the expectation value continues to change even after the field is turned off); and (2) simultaneous back-to-back motion with the field couples only at second order in time. Nevertheless, the analysis of the local control method led to insights in choosing an appropriate gauge and the form of the objective.

Although the various control algorithms gave superficially different optimal fields, on closer analysis we were able to identify a similar mechanism underlying all the optimal fields based on a two-step procedure. The mechanism is as follows: (1) the electrons are first pushed into the same direction by the field, while they are still close to each other, i.e. front-to-back motion; (2) after the field turns off, the electrons are simultaneously attracted by the nucleus and repel each other. This finally leads to the desired back-to-back motion. To enable step (1), the potential induced by the field must be stronger than both the Coulomb repulsion of the electrons and the nuclear Coulomb attraction. Both steps can be repeated several times. The mechanism displays a nontrivial interplay between the electron-field interaction at a certain intensity range, which drives the electrons to the direction opposite to our goal, and the electron-nuclear and electron-electron interactions, which are both required for steering the displaced electrons to the final back-to-back motion. Remarkably, we obtained the same results using classical propagation and optimization. The essentials of this mechanisms are thus a classical effect.

All results have been performed with our new dynamically pruned DVR (DP-DVR),⁴⁹⁻⁵¹ where a non-direct-product basis is employed that is adapted to the shape of the wavepacket in coordinate space at each time step. Compared to standard, e.g., FFT-based dynamics on a direct-product grid, this approach can be orders of magnitude faster and thus enabled the very quick simulations that were needed to perform this study.

ACKNOWLEDGMENTS

We are thankful to Daniel Reich for helpful discussion about quantum control algorithms and Norio Takemoto for helpful discussions in the beginning of this project. H. R. L. is thankful to Timm Faulwasser and Karl Worthmann for introducing him to classical optimization problems and algorithms during a summer school of the Studienstiftung des deutschen Volkes. H. R. L. acknowledges financial support from the Fonds der Chemischen Industrie and the Studienstiftung des deutschen Volkes.

Financial support from the Israel Science Foundation (1094/16) and the German-Israeli Foundation for Scientific Research and Development (GIF) are gratefully acknowledged.

CONFLICT OF INTEREST

The authors have no conflicts to disclose.

DATA AVAILABILITY STATEMENT

The data that support the findings of this study are available from the corresponding author upon reasonable request.

SUPPLEMENTARY MATERIAL

See supplementary material for more numerical details on our DP-DVR simulation method (Section A) and on the various control algorithms (Section B), for additional control results (Section C), and for spectrograms of the optimized pulses presented here (Section D).

- ¹C. F. de Morisson Faria and X. Liu, *J. Mod. Opt.* **58**, 1076 (2011).
- ²A. Staudte, C. Ruiz, M. Schöffler, S. Schössler, D. Zeidler, T. Weber, M. Meckel, D. M. Villeneuve, P. B. Corkum, A. Becker, and R. Dörner, *Phys. Rev. Lett.* **99**, 263002 (2007).
- ³D. Azoury, M. Krüger, G. Orenstein, H. R. Larsson, S. Bauch, B. D. Bruner, and N. Dudovich, *Nat. Commun.* **8**, 1453 (2017).
- ⁴K. Ueda, E. Sokell, S. Schippers, F. Aumayr, H. Sadeghpour, J. Burgdörfer, C. Lemell, X.-M. Tong, T. Pfeifer, F. Calegari, A. Palacios, F. Martin, P. Corkum, G. Sansone, E. V. Gryzlova, A. N. Grum-Grzhimailo, M. N. Piancastelli, P. M. Weber, T. Steinle, K. Amini, J. Biegert, N. Berrah, E. Kukk, R. Santra, A. Müller, D. Dowek, R. R. Lucchese, C. W. McCurdy, P. Bolognesi, L. Avaldi, T. Jahnke, M. S. Schöffler, R. Dörner, Y. Mairesse, L. Nahon, O. Smirnova, T. Schlathölter, E. E. B. Campbell, J.-M. Rost, M. Meyer, and K. A. Tanaka, *J. Phys. B* **52**, 171001 (2019).
- ⁵K. Amini, J. Biegert, F. Calegari, A. Chacón, M. F. Ciappina, A. Dauphin, D. K. Efimov, C. Figueira de Morisson Faria, K. Giergiel, P. Gniewek, A. S. Landsman, M. Lesiuk, M. Mandrysz, A. S. Maxwell, R. Moszyński, L. Ortman, J. Antonio Pérez-Hernández, A. Picón, E. Pisanty, J. Prauzner-Bechcicki, K. Sacha, N. Suárez, A. Zaïr, J. Zakrzewski, and M. Lewenstein, *Rep. Prog. Phys.* **82**, 116001 (2019).
- ⁶R. Dörner, T. Weber, M. Weckenbrock, A. Staudte, M. Hattass, H. Schmidt-Böcking, R. Moshhammer, and J. Ullrich, in *Advances In Atomic, Molecular, and Optical Physics*, Vol. 48, edited by B. Bederson and H. Walther (Academic Press, 2002) Chap. Multiple Ionization in Strong Laser Fields, pp. 1–34.
- ⁷W. Becker and H. Rottke, *Contemp. Phys.* **49**, 199 (2008).
- ⁸A. H. Winney, S. K. Lee, Y. F. Lin, Q. Liao, P. Adhikari, G. Basnayake, H. B. Schlegel, and W. Li, *Phys. Rev. Lett.* **119**, 123201 (2017).
- ⁹X. Li, J. Yu, H. Xu, X. Yu, Y. Yang, Z. Wang, P. Ma, C. Wang, F. Guo, Y. Yang, S. Luo, and D. Ding, *Phys. Rev. A* **100**, 013415 (2019).
- ¹⁰A. Kramida, Yu. Ralchenko, J. Reader, and NIST ASD Team, NIST Atomic Spectra Database (ver. 5.5.2), [Online]. Available: <https://physics.nist.gov/asd>. National Institute of Standards and Technology, Gaithersburg, MD. (2018).
- ¹¹L. Zhang, X. Xie, S. Roither, Y. Zhou, P. Lu, D. Kartashov, M. Schöffler, D. Shafir, P. B. Corkum, A. Baltuška, A. Staudte, and M. Kitzler, *Phys. Rev. Lett.* **112**, 193002 (2014).
- ¹²A. S. Maxwell and C. F. d. M. Faria, *Phys. Rev. Lett.* **116**, 143001 (2016).
- ¹³A. Rudenko, L. Foucar, M. Kurka, T. Ergler, K. U. Kühnel, Y. H. Jiang, A. Voitkiv, B. Najjari, A. Kheifets, S. Lüdemann, T. Havermeier, M. Smolarski, S. Schössler, K. Cole, M. Schöffler, R. Dörner, S. Düsterer, W. Li, B. Keitel, R. Treusch, M. Gensch, C. D. Schröter, R. Moshhammer, and J. Ullrich, *Phys. Rev. Lett.* **101**, 073003 (2008).
- ¹⁴R. Moshhammer, Y. H. Jiang, L. Foucar, A. Rudenko, T. Ergler, C. D. Schröter, S. Lüdemann, K. Zrost, D. Fischer, J. Titze, T. Jahnke, M. Schöffler, T. Weber, R. Dörner, T. J. M. Zouros, A. Dorn, T. Ferger, K. U. Kühnel, S. Düsterer, R. Treusch, P. Radcliffe, E. Plönjes, and J. Ullrich, *Phys. Rev. Lett.* **98**, 203001 (2007).
- ¹⁵Y. H. Jiang, A. Rudenko, M. Kurka, K. U. Kühnel, L. Foucar, T. Ergler, S. Lüdemann, K. Zrost, T. Ferger, D. Fischer, A. Dorn, J. Titze, T. Jahnke, M. Schöffler, S. Schössler, T. Havermeier, M. Smolarski, K. Cole, R. Dörner, T. J. M. Zouros, S. Düsterer, R. Treusch, M. Gensch, C. D. Schröter, R. Moshhammer, and J. Ullrich, *J. Phys. B* **42**, 134012 (2009).
- ¹⁶G. Katsoulis, A. Hadjipittas, B. Bergues, M. Kling, and A. Emmanouilidou, *Phys. Rev. Lett.* **121**, 263203 (2018).
- ¹⁷M. Kübel, K. J. Betsch, N. G. Kling, A. S. Alnaser, J. Schmidt, U. Kleineberg, Y. Deng, I. Ben-Itzhak, G. G. Paulus, T. Pfeifer, J. Ullrich, R. Moshhammer, M. F. Kling, and B. Bergues, *New J. Phys.* **16**, 033008 (2014).
- ¹⁸A. Becker and F. H. M. Faisal, *Phys. Rev. A* **50**, 3256 (1994).
- ¹⁹S. Chen, C. Ruiz, and A. Becker, *Phys. Rev. A* **82**, 033426 (2010).
- ²⁰A. Liu and U. Thumm, *Phys. Rev. A* **89**, 063423 (2014).
- ²¹G. D. Borisova, V. Stooß, A. Dingeldey, A. Kaldun, T. Ding, P. Birk, M. Hartmann, T. Heldt, C. Ott, and T. Pfeifer, *J. Phys. Commun.* **4**, 055012 (2020).
- ²²B. Bergues, M. Kübel, N. G. Johnson, B. Fischer, N. Camus, K. J. Betsch, O. Herrwerth, A. Senftleben, A. M. Saylor, T. Rathje, T. Pfeifer, I. Ben-Itzhak, R. R. Jones, G. G. Paulus, F. Krausz, R. Moshhammer, J. Ullrich, and M. F. Kling, *Nat. Commun.* **3**, 813 (2012).
- ²³J. M. Ngoko Djiokap, N. L. Manakov, A. V. Meremianin, S. X. Hu, L. B. Madsen, and A. F. Starace, *Phys. Rev. Lett.* **113**, 223002 (2014).
- ²⁴Y. Liu, S. Tschuch, A. Rudenko, M. Dürr, M. Siegel, U. Morgner, R. Moshhammer, and J. Ullrich, *Phys. Rev. Lett.* **101**, 053001 (2008).
- ²⁵J. S. Prauzner-Bechcicki, K. Sacha, B. Eckhardt, and J. Zakrzewski, *Phys. Rev. Lett.* **98**, 203002 (2007).
- ²⁶M. Lein, E. K. U. Gross, and V. Engel, *Phys. Rev. Lett.* **85**, 4707 (2000).
- ²⁷E. Eremina, X. Liu, H. Rottke, W. Sandner, A. Dreischuh, F. Lindner, F. Grasbon, G. G. Paulus, H. Walther, R. Moshhammer, B. Feuerstein, and J. Ullrich, *J. Phys. B* **36**, 3269 (2003).
- ²⁸D. A. Horner, T. N. Rescigno, and C. W. McCurdy, *Phys. Rev. A* **77**, 030703 (2008).
- ²⁹E. Fomouo, P. Antoine, B. Piraux, L. Malegat, H. Bachau, and R. Shakeshaft, *J. Phys. B* **41**, 051001 (2008).
- ³⁰D. J. Tannor and S. A. Rice, *J. Chem. Phys.* **83**, 5013 (1985).
- ³¹R. Kosloff, S. A. Rice, P. Gaspard, S. Tersigni, and D. J. Tannor, *Chem. Phys.* **139**, 201 (1989).
- ³²D. J. Tannor and A. Bartana, *J. Phys. Chem. A* **103**, 10359 (1999).
- ³³P. Doria, T. Calarco, and S. Montangero, *Phys. Rev. Lett.* **106**, 190501 (2011).
- ³⁴R. E. Goetz, M. Merkel, A. Karamatskou, R. Santra, and C. P. Koch, *Phys. Rev. A* **94**, 023420 (2016).
- ³⁵R. Heck, O. Vuculescu, J. J. Sørensen, J. Zoller, M. G. Andreassen, M. G. Bason, P. Ejlertsen, O. Eliasson, P. Haikka, J. S. Laustsen, L. L. Nielsen, A. Mao, R. Müller, M. Napolitano, M. K. Pedersen,

- A. R. Thorsen, C. Bergenholtz, T. Calarco, S. Montangero, and J. F. Sherson, *Proc. Nat. Acad. Sci.* **115**, E11231 (2018).
- ³⁶A. Larrouy, S. Patsch, R. Richaud, J.-M. Raimond, M. Brune, C. P. Koch, and S. Gleyzes, *Phys. Rev. X* **10**, 021058 (2020).
- ³⁷E. Papastathopoulos, M. Strehle, and G. Gerber, *Chem. Phys. Lett.* **408**, 65 (2005).
- ³⁸M. Sukharev, E. Charron, and A. Suzor-Weiner, *Phys. Rev. A* **66**, 053407 (2002).
- ³⁹R. E. Goetz, A. Karamatskou, R. Santra, and C. P. Koch, *Phys. Rev. A* **93**, 013413 (2016).
- ⁴⁰J. B. Schönborn, P. Saalfrank, and T. Klamroth, *J. Chem. Phys.* **144**, 044301 (2016).
- ⁴¹I. Schaefer and R. Kosloff, *Phys. Rev. A* **101**, 023407 (2020).
- ⁴²H. R. Larsson, S. Bauch, L. K. Sørensen, and M. Bonitz, *Phys. Rev. A* **93**, 013426 (2016).
- ⁴³S. Bauch, H. R. Larsson, C. Hinz, and M. Bonitz, *J. Phys.: Conf. Ser.* **696**, 012008 (2016).
- ⁴⁴C. Yu and L. B. Madsen, *Phys. Rev. A* **94** (2016).
- ⁴⁵M. S. Pindzola, G. M. Laurent, and J. P. Colgan, *J. Phys. B* **50**, 185601 (2017).
- ⁴⁶A. Marinelli, D. Ratner, A. A. Lutman, J. Turner, J. Welch, F.-J. Decker, H. Loos, C. Behrens, S. Gilevich, A. A. Miahnahri, S. Vetter, T. J. Maxwell, Y. Ding, R. Coffee, S. Wakatsuki, and Z. Huang, *Nat. Commun.* **6**, 6369 (2015).
- ⁴⁷C. Emma, X. Xu, A. Fisher, R. Robles, J. P. MacArthur, J. Cryan, M. J. Hogan, P. Musumeci, G. White, and A. Marinelli, *APL Photonics* **6**, 076107 (2021).
- ⁴⁸U. Bergmann, J. Kern, R. W. Schoenlein, P. Wernet, V. K. Yachandra, and J. Yano, *Nat. Rev. Phys.* **3**, 264 (2021).
- ⁴⁹H. R. Larsson, B. Hartke, and D. J. Tannor, *J. Chem. Phys.* **145**, 204108 (2016).
- ⁵⁰H. R. Larsson, J. Riedel, J. Wei, F. Temps, and B. Hartke, *J. Chem. Phys.* **148**, 204309 (2018).
- ⁵¹D. J. Tannor, S. Machnes, E. Assémat, and H. R. Larsson, “Phase space vs. coordinate space methods: Prognosis for large quantum calculations,” in *Advances in Chemical Physics*, Vol. 163 (John Wiley & Sons, Inc., 2018) pp. 273–323.
- ⁵²H. R. Larsson and D. J. Tannor, *J. Chem. Phys.* **147**, 044103 (2017).
- ⁵³Throughout, we use atomic units ($m_e = e = 4\pi\epsilon_0 = a_0 = 2|E_{\text{Ryd}}| = 1$) unless indicated otherwise.
- ⁵⁴E. Assémat, S. Machnes, and D. Tannor, “Double ionization of Helium from a phase space perspective,” (2015), arXiv:1502.05165.
- ⁵⁵B. Bransden and C. Joachain, *Physics of Atoms & Molecules*, 2nd ed. (Dorling Kindersley, 2006).
- ⁵⁶L. B. Madsen, *Phys. Rev. A* **65**, 053417 (2002).
- ⁵⁷Y.-C. Han and L. B. Madsen, *Phys. Rev. A* **81**, 063430 (2010).
- ⁵⁸It may also happen that the larger fraction of the doubly ionized wavepacket is in D_1 but then, typically its main component is not along the $u = 0$ line, indicating not a true back-to-back motion.
- ⁵⁹D. J. Tannor, *Introduction to Quantum Mechanics: A Time-Dependent Perspective*, 1st ed. (University Science Books, 2007).
- ⁶⁰G. G. Balint-Kurti, S. Zou, and A. Brown, in *Advances in Chemical Physics*, Vol. 138 (John Wiley & Sons, Inc., 2008) Chap. Optimal Control Theory for Manipulating Molecular Processes, pp. 43–94.
- ⁶¹J. Werschnik and E. K. U. Gross, *J. Phys. B* **40**, R175 (2007).
- ⁶²To simplify notation, we drop the hats in the coordinate operators \hat{u} and \hat{v} . It will be clear from the context whether operators are meant or not.
- ⁶³Local control results are presented in Section C.1 of the supplementary material.
- ⁶⁴V. Engel, C. Meier, and D. J. Tannor, in *Advances in Chemical Physics*, Vol. 141 (John Wiley & Sons, Inc., 2009) Chap. Local Control Theory: Recent Applications to Energy and Particle Transfer Processes in Molecules, pp. 29–101.
- ⁶⁵Y. Ohtsuki, Y. Yahata, H. Kono, and Y. Fujimura, *Chem. Phys. Lett.* **287**, 627 (1998).
- ⁶⁶Local control results are presented in Section C.1 of the supplementary material.
- ⁶⁷Here, global optimization means not an optimization to a global minimum but that the field is optimized *globally*.
- ⁶⁸A. R. Conn, K. Scheinberg, and L. N. Vicente, *Introduction to Derivative-Free Optimization*, 1st ed. (SIAM, 2009).
- ⁶⁹C. Gollub, M. Kowalewski, and R. de Vivie-Riedle, *Phys. Rev. Lett.* **101**, 073002 (2008).
- ⁷⁰M. Schröder and A. Brown, *New J. Phys.* **11**, 105031 (2009).
- ⁷¹V. F. Krotov, *Global Methods in Optimal Control Theory*, 1st ed. (Dekker, 1996).
- ⁷²D. J. Tannor, V. Kazakov, and V. Orlov, in *Time-Dependent Quantum Molecular Dynamics*, edited by J. Broeckhove and L. Lathouwers (Springer, 1992) Chap. Control of photochemical branching: Novel procedures for finding optimal pulses and global upper bounds, pp. 347–360.
- ⁷³R. Eitan, M. Mundt, and D. J. Tannor, *Phys. Rev. A* **83**, 053426 (2011).
- ⁷⁴P. Deuffhard and F. Bornemann, *Numerische Mathematik 2: Gewöhnliche Differentialgleichungen*, 3rd ed. (de Gruyter, 2008).
- ⁷⁵J. A. E. Andersson, J. Gillis, G. Horn, J. B. Rawlings, and M. Diehl, *Math. Prog. Comp.* **11**, 1 (2019).
- ⁷⁶See Section B.2 in the supplementary material for details on the restriction on the maximal field amplitude.
- ⁷⁷M. Brehm, *Analyzing Trajectories from Molecular Simulation*, Ph.D. thesis, University of Leipzig (2013).
- ⁷⁸S. Ruhman and R. Kosloff, *J. Opt. Soc. Am. B* **7**, 1748 (1990).
- ⁷⁹J. Cao and K. R. Wilson, *J. Chem. Phys.* **107**, 1441 (1997).
- ⁸⁰S. Ruetzel, C. Stolzenberger, S. Fechner, F. Dimler, T. Brixner, and D. J. Tannor, *J. Chem. Phys.* **133**, 164510 (2010).
- ⁸¹M. J. D. Powell, *Acta Numer.* **7**, 287–336 (1998).
- ⁸²M. J. D. Powell, *Cambridge NA Report NA200906* (2009).
- ⁸³T. Weise, *Global Optimization Algorithms*, 3rd ed. (www.it-weise.de, 2011).
- ⁸⁴W. P. Schleich, *Quantum Optics in Phase Space*, 1st ed. (Wiley-VCH, 2001).
- ⁸⁵S. Fechner, F. Dimler, T. Brixner, G. Gerber, and D. J. Tannor, *Opt. Express* **15**, 15387 (2007).
- ⁸⁶S. Machnes, E. Assémat, H. R. Larsson, and D. J. Tannor, *J. Phys. Chem. A* **120**, 3296 (2016).
- ⁸⁷N. Takemoto, A. Shimshovitz, and D. J. Tannor, *J. Chem. Phys.* **137**, 011102 (2012).
- ⁸⁸Note that the field in the length gauge would have components with both positive and negative values. Note further that, due to symmetry of the potential in u , the overall sign of the field does not matter.
- ⁸⁹The larger momentum components for $v = 0$ are due to the form of the potential and as such are “ground state quantities” and not very interesting for this study.
- ⁹⁰J. M. Bowman, B. Gazdy, and Q. Sun, *J. Chem. Phys.* **91**, 2859 (1989).
- ⁹¹W. H. Miller, W. L. Hase, and C. L. Darling, *J. Chem. Phys.* **91**, 2863 (1989).
- ⁹²T. Kjellsson, S. Selstø, and E. Lindroth, *Phys. Rev. A* **95**, 043403 (2017).